



Near surface electric field enhancement: Pyridinic-N rich few-layer graphene encapsulating cobalt catalysts as highly active and stable bifunctional ORR/OER catalyst for seawater batteries

Seonghee Kim^{a,1}, Seulgi Ji^{d,1}, Hyeonsu Yang^a, Hyunjee Son^a, Heechae Choi^{d,*}, Jun Kang^{b,c,**}, Oi L. Li^{a,*}

^a Department of Materials Science and Engineering, Pusan national University, 2 Busandaehak-ro 63beon-gil, Geumjeong-gu, Busan 46241, Republic of Korea

^b Division of Marine system Engineering, Korea Maritime and Ocean University, 727, Taejong-ro, Yeongdo-gu, Busan, 49112, Republic of Korea

^c Interdisciplinary Major of Maritime AI Convergence, Korea Maritime and Ocean University, Busan, 49112, Republic of Korea

^d Theoretical Materials & Chemistry Group, Institute of Inorganic Chemistry, University of Cologne, Greinstraße 6, 50939, Cologne, Germany

ARTICLE INFO

Keywords:

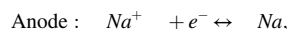
Nitrogen doped carbon
Cobalt core shell
Seawater battery
E-field calculation
Electrocatalyst

ABSTRACT

Rechargeable seawater batteries (SWBs) are recently considered as a new approach in next-generation energy storage. However, the presence of chloride ions inhibits the performance and durability of the air cathode electrocatalysts. This study is the first research to report the effect of the built-in electric field on corrosion prevention via Cl⁻ repulsion. Our DFT model successfully demonstrated the near-surface charge transfer at the interface of cobalt core and pyridinic-N graphene (Co (fcc)/N-Gr) strongly contributed to advanced catalytic activity and selectively Cl⁻ repulsion in seawater electrolyte. Experimentally, the structure of a few layered N-doped graphene encapsulated cobalt (Co 4 mmol-N/C) showed superior catalytic activity in both alkaline (ΔE ($E_{j=10} - E_{1/2}$) = 0.774 V) and seawater (ΔE = 1.167 V). Furthermore, Co 4 mmol-N/C demonstrated an extremely low overpotential (0.56 V) at 0.1 mA and presented superior stability for 100 h in a rechargeable SWB.

1. Introduction

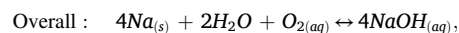
Research and development have been performed on several types of energy systems, including metal-air batteries and fuel cells, to meet the high demand for sustainable energy that can reduce the use of fossil fuels and their accompanying environmental problems [1–5]. Recently, rechargeable seawater batteries (SWBs) attract significant research attention owing to the ubiquity of Na⁺ ions in seawater as a cathodic active material for the electrochemical sodium exchange reaction. The half-cell and overall reactions and their corresponding theoretical potentials in seawater are as follow:



$$E^\circ = -2.25 \text{ V vs. RHE} \quad (1)$$



$$E^\circ = 1.228 \text{ V vs. RHE} \quad (2)$$



$$E^\circ = 3.478 \text{ V vs. Na/Na}^+ \quad (3)$$

Based on Eq. 3, the theoretical cell voltage of the SWBs is approximately 3.48 V vs. Na/Na⁺ at pH 8 [6,7]. The SWBs has the most important advantage on sustainability, which applies seawater in an almost infinite amount as a cathodic material and is safer than other lithium- or sodium-based electrical energy storage systems. Up-to-date, SWBs has been developed from small systems designed for buoys and life jackets to industrial-scale energy storage systems [8–10]. However, the development of SWBs is still at its early stage because of the complexity of the seawater components as electrolytes. Briefly, the SWBs performance is often determined by the oxygen reactions at the cathode, where the oxygen reduction reaction (ORR) determines the discharge

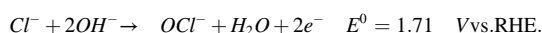
* Corresponding authors.

** Corresponding author at: Division of Marine system Engineering, Korea Maritime and Ocean University, 727, Taejong-ro, Yeongdo-gu, Busan, 49112, Republic of Korea.

E-mail addresses: h.choi@uni-koeln.de (H. Choi), junkang@kmou.ac.kr (J. Kang), helenali@pusan.ac.kr (O.L. Li).

¹ equally contributed as a 1-st author

voltage and the oxygen evolution reaction (OER) dictates the charging voltage. In general, platinum-group metals (PGMs) and their alloys are reported as high-efficient ORR/OER electrocatalysts. However, the performance of PGM catalysts is greatly hindered by the presence of chloride ions (Cl^-) in seawater followed by severe corrosion of the electrocatalysts during long-term operation. Specifically, Cl^- can easily block the metal active sites and limit the adsorption of O_2 molecules, especially in Pt-based materials. The adsorption of Cl^- on the metal surface decreases the catalytic activity and reduces the reaction kinetics by disturbing the breakage of the O–O bonds during the ORR, therefore, changes the 4-electron to a 2-electron reaction [11,12]. In addition, the chlorine oxidation reaction (CIER) competes with the OER and might generate chlorine by-products during charging of the SWBs [13]. Considering the CIER reaction at pH 8 and a total chlorine concentration of 0.54 M in seawater at room temperature, the formation of hypochlorite (OCl^-) might proceed as follows:



Although OER is thermodynamically more favorable than CIER in natural seawater, the electrocatalyst must be decorated by a chloride-resistant layer to prevent accelerated corrosion during the OER reaction. Hence, developing a stable bi-functional ORR/OER catalyst with high Cl^- resistance is the most urgent issue to ensure the practical application of SWBs as novel energy storage systems [14–17].

To overcome these challenges, graphene encapsulated cobalt catalyst (Co-C) is considered as one of the most promising candidates due to its high activity and chemical stability owing to the protective carbon layer [18]. Suh et al. designed a hierarchically structured graphene-carbon nanotube-cobalt hybrid electrocatalyst (S-rGO-CNT-Co) as an efficient seawater cathodic electrocatalyst. The reported S-rGO-CNT-Co was composed of tubular-structured CNTs with partially encapsulated 10–30 nm Co nanoparticles, while the metal loading of Co was as high as 55.1 wt%. The hybrid nanostructure of Co-C with thin graphene layers worked as the protective layer to prevent adsorption of the Cl^- on the cobalt core and enhanced the chemical stability. The S-rGO-CNT-Co electrocatalyst showed a superior charge voltage (3.42 V) and discharge voltage (3.00 V) at 0.01 mA cm^{-2} . Although the reported Co-based electrocatalysts demonstrated remarkable performance, the discharge performance was still inferior to that of 20 wt% Pt/C catalysts in SWBs. Also, since the cobalt active sites were not entirely encapsulated within the graphene shell, S-rGO-CNT-Co rapidly degraded in SWBs even at a low current and the cathode catalysts still suffered from accelerated corrosion [19]. Thus, a better modification of graphene encapsulated cobalt catalysts is required to improve the chemical stability in seawater electrolyte. In particular, it is crucial to design more appropriate protective layer to repel corrosive Cl^- ions.

The activities of heterogeneous catalysts are determined mostly by three key factors: adsorption energies, reaction intermediates, carrier and ion transport. In many previous works, DFT calculation was employed to predict and analyse the surface reaction kinetics and metallic properties of heterogeneous materials by computing electron density of states (DOS) and adsorption energies. However, other factors such as carrier and ion transport has been mostly overlooked even though the change in local pH value has been recently reported to significantly alter catalysts' activities [20,21]. Also, the electrostatic potential barrier formed by the electrical double layer greatly affects the charge transfer [22]. Therefore, the overall catalytic activity can be controlled by the electrostatic potential barrier at a catalyst surface. With the same principle, the corrosion rate of a catalyst surface, which is a function of chemical potential change by reaction, is also controllable with manipulating the surface electrostatic potential. Among all types of nitrogen-carbon chemical bonding, pyridinic-N provides the highest negative charge of the carbon surface [23,24]. The enhanced surface electric charge is expected to repel negative Cl^- ions selectively, which could hinder the CIER and increase the chemical tolerance by preventing

adsorption of Cl^- on the catalyst surface.

In this study, the pyridinic-N doped few layers graphene encapsulating cobalt catalyst (Co-N/C) was proposed as highly active and Cl^- -resistance bi-functional electrocatalysts for rechargeable SWBs. For the first time, this original work has utilized a properly-engineered interface dipole moments of cobalt-graphene heterojunctions to block the negative Cl^- ions by Coulomb repulsion. Firstly, based on the density functional theory (DFT), the energy diagram showed that the catalytic activity of encapsulated cobalt nanoparticle was greatly enhanced by pyridinic-N doping into the graphene layer. The model also proved that pyridinic-N doped graphene layer significantly promoted and strengthened the electric field of the Co-N/C surface. The highly negative surface charge contributed to strong repulsion of Cl^- and prevented the surface poisoning from harsh seawater electrolyte. Furthermore, we had fabricated the proposed pyridinic-N doped few layers graphene encapsulated cobalt catalyst (Co-N/C) via plasma engineering and experimentally evaluated the performance of our electrocatalysts in a rechargeable SWB. The Co 4 mmol-N/C catalysts consisted of extremely high density (48 wt%) of nano-sized (20–40 nm) cobalt nanoparticles, which were well-dispersed and totally embedded into few layers of pyridinic-N doped graphene shell. Owing to the enhanced negative electric field on the pyridinic-N graphene surface, Co 4 mmol-N/C showed superior catalytic activity and high resistance to Cl^- . As a result, Co 4 mmol-N/C demonstrated an extremely low overpotential (0.56 V) during the 1st charge-discharge cycle in a rechargeable SWBs, and small increase of voltage gap (~10%) after a continuous charge-discharge cycle for 100 h. After the durability test, the peak corresponding to the pyridinic-N group on the protective N-doped graphene layer has transformed to pyrrolic-N, suggesting that the pyridinic-N group has high affinity to protect the cobalt active site from the corrosive environment. The above result provides a new design direction and synthesis approach to develop high performance and stable cathodic electrocatalyst for seawater batteries in near future. [25–27]

2. Experimental

2.1. DFT calculation

DFT calculations were performed using the Vienna ab initio simulation package (VASP). The projector augmented wave method (PAW) was used to describe the interaction between valence and core electrons. The general gradient approximation (GGA) with the Perdew, Burke, and Ernzerhof exchange-correlation functional (PBE) was employed for the plane-basis wave expansion. The Brillouin zone was sampled by a Gamma-centered k-points grid of $2 \times 2 \times 1$ to optimize the cell parameters and the kinetic energy was cut-off at 400 eV. The energy convergence criteria in the self-consistent field were set to 10^{-6} eV. All geometry structures were fully relaxed until Hellman-Feynman forces reached 0.1 eV \AA^{-1} . To understand the effects of the interfacial structures on the catalytic activity and Cl^- -resistance properties, we compared two different types of Co-graphene heterojunction structures: (1) Co(fcc) phases with graphene (Gr) and (2) Co(fcc) with pyridinic-N doped graphene (N-Gr), in which three N atoms are embedded on a single graphene layer. The supercell dimensions for Co(fcc)@Gr and Co(fcc)@N-Gr were constructed as $9.96 \text{ \AA} \times 9.96 \text{ \AA} \times 22.2 \text{ \AA}$, where the vacuum layers were placed along the c axis to avoid the interactions between the adjacent periodic supercells. (Fig. S1).

2.2. Preparation of pyridinic-N few-layer graphene encapsulating cobalt catalysts

The pyridinic-N few-layer graphene encapsulating cobalt catalysts were synthesized via plasma engineering. First, different amounts (2, 3, and 4 mmol) of cobalt chloride hexahydrate were dissolved into a mixture of 50 mL of pyridine (purity > 99%, Junsei Chemical Co., Ltd, Tokyo, Japan) and 50 mL dimethylformamide (DMF) solution by

magnetic stirring for 1 h to obtain the well-mixed precursor solution. Then, plasma was discharged into the precursor through a pair of graphite electrodes (diameter: 2 mm) using a bipolar pulse power (MPP-HV02, Kurita Seisakusho, Kyoto, Japan). The discharge was strictly maintained at a voltage of 1.6 kV, frequency of 50 kHz, and pulse width of 1.2 μ s for 10 min to obtain 100 mg of catalyst. The catalyst powder was filtered by a Φ 55-mm polytetrafluoroethylene filter and washed with deionized water until effluent turned transparent. The catalyst powder was dried in an oven for 10 h at 80 °C. Finally, the as-prepared catalysts were annealed in a tube furnace at 700 °C with ramping at 2 °C/min under N_2 flow of 1.5 mL min⁻¹ and then cooled to room temperature for further testing.

2.3. Characterization of the structural and chemical properties

The morphology and structure properties of plasma-engineered Co-N/C electrocatalysts were analyzed by X-ray diffraction (XRD, Rigaku, Ultima Ilima a Ilima by X-ray diffraction (XRD, sts were analyzed Thermo Fisher Scientific, TALOS F200X, Seoul, Korea) at the National Nanofab Center (Daejeon, Korea). TGA was performed using a thermal analyser (TA, PerkinElmer, STA6000, Seoul, Korea) To determine the calcination of the catalysts. The surface area and pore area of the synthesized catalysts were determined by the nitrogen adsorption-desorption method (Brunauer-Emmett-Teller, Shimadzu, Tristar-Tristar-Tokyo, Japan). The chemical composition was characterized by X-ray photoelectron spectroscopy (XPS, JEOL, JPS-9010MC, Tokyo, Japan) at the Korea Basic Science Institute (Pusan, Korea). The precise concentration of cobalt in the as-synthesized catalysts was determined by inductively coupled plasma-optical emission spectrometer (ICP-OES, PerkinElmer, Optima 8300, USA).

2.4. Electrochemical measurements

An electrochemical potentiostat (Biologic, VSP, Grenoble, France) was used to analyse the catalytic activity of the synthesized 2–4 mmol Co-N/C and 20 wt% Pt/C (Fuelcell store, 20% Platinum on Carbon XC-72) in 0.1 M KOH and artificial seawater electrolyte (AF Perfect Water, Aquaforest, Brzesko, Poland). The catalyst ink was composed of well-ground powder catalyst (8 mg) in a mixed solution of distilled water (480 μ L), ethanol (480 μ L), and Nafion®117 solution (40 μ L), and then ultrasonicated for 30 min until the catalyst powder were well-dispersed inside the catalyst ink. Then, the catalyst ink (800 μ g cm⁻²) was dropped on a well-polished glassy carbon disk electrode (4 mm diameter) as the working electrode. A platinum coil counter electrode was used together with a Hg/HgO (1 M NaOH) reference electrode for the 0.1 M KOH electrolyte, or a Ag/AgCl (1 M KCl) reference electrode for the seawater electrolyte to establish a standard three-electrode cell system. The catalytic activity of ORR was measured by linear sweep voltammetry (LSV) at a scan rate of 5 mV s⁻¹, rotating speed of 1600 rpm, and a potential range from 0.2 to 1.0 V vs. RHE in 0.1 M KOH, and from 1.0 to 0.2 V vs. RHE in seawater electrolyte. Cyclic voltammetry (CV) was performed at 50 mV s⁻¹ over a potential range from 0.1 to 1.2 V vs. RHE in 0.1 M KOH, and from -0.2 to 1.0 V vs. RHE in seawater electrolyte. The catalytic activity of OER was measured by linear sweep voltammetry (LSV) in N_2 -saturated electrolyte at a scan rate of 5 mV s⁻¹, a rotating speed of 1600 rpm, and potential ranges between 1.2 and 1.8 V and 1.2–2.0 V vs. RHE in 0.1 M KOH and artificial seawater electrolyte, respectively.

2.5. Preparation of seawater battery

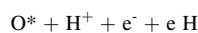
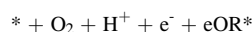
The cathode for the seawater battery was fabricated from a slurry containing 9 mg of Co 4 mmol-N/C or 20 wt% Pt/C with 1 mg polyvinylidene fluoride (PVDF) in 100 μ L of N-methyl-2-pyrrolidone (NMP). Carbon felt (company, model size = 2 cm²) was applied as the current collector and preheated before coating at 500 °C for 2 h in ambient air

with a ramping rate of 2 °C/min to increase the hydrophilicity of the surface. The catalyst slurry was then coated on the carbon felt substrate at approximately 4.5 mg/cm² of catalyst loading and dried at 80 °C for 24 h in an oven [28]. The mass loading of ~ 4.5 mg/cm² was estimated by the weight difference of the pre-heated carbon felt before and after coating the active materials. A flow-type seawater battery jig was constructed to analyse the fabricated cathode, which was placed in direct contact with the seawater. The anode was separated by NASICON membrane to prevent from contacting the seawater. A Ti wire was connected to 2 cm² of carbon felt as a current collector. After assembling the coin-type anode cell and cathode, 200 mL of seawater was used as the cathodic active material. The concentration of DO in seawater electrolyte was measured by a water quality meter (Thermo Scientific Orion, model: Orion star A216) and maintained at approximately 10 mg/L throughout the SWBs test. The performance of the flow-type SWB was evaluated at room temperature. Galvanostatic charge-discharge cycling was performed at 0.1 mA for 1 h in each cycle.

3. Result and discussion

3.1. Modeling of cobalt (fcc)/N doped carbon via DFT

To develop a suitable model for Co-N/C electrocatalysts for seawater application, we first applied the free energy diagram to compare the ORR catalytic activities at an intermediate pH. The Gibbs free energy (ΔG) of ORR on Gr and pyridinic N-Gr capsulating Co(fcc) phases are calculated to investigate the effects of cobalt phase and nitrogen doping in cobalt-graphene heterojunctions on the surface reaction energetics (Fig. 1) in four elementary ORR steps [29]:



Based on the ORR steps above, the reaction free energy ΔG_i ($i = 1, 2, 3, 4$) for each ORR step is calculated using the expression,

$$\Delta G_i = \Delta E + \Delta E_{ZPE} - T\Delta S + \Delta G_U + \Delta G_{pH} \quad (6)$$

where ΔE is the total energy change derived from DFT calculations, ΔE_{ZPE} is the zero-point energy correction, T is the absolute temperature (300 K), ΔS is the changes of entropies of the adsorbates. In the bias related term of Eq. (2), $\Delta G_U = -neU$, n is the number of proton-electron transferred pairs, the e is the number of involved electrons and U is the potential at the electrode [30]. The ΔG_{pH} term in eqn(X) is $-k_B T \ln 10 \times pH$ and k_B is the Boltzmann constant. In this work, as the oxygen reduction reaction occurs in seawater, pH = 8 was considered in the calculation. The theoretical overpotential (η_{ORR}) at pH = 8 was calculated using the following equation,

$$\eta_{ORR} = 0.81 \text{ V} - \frac{\min\{\Delta G_1, \Delta G_2, \Delta G_3, \Delta G_4\}}{e} \quad (7)$$

where the minimum value of ΔG_i ($i = 1, 2, 3, 4$) is the minimum potential at which all elementary steps in ORR are exothermic [31]. When no bias is applied ($U = 0$ V), all the electron-transfer steps are exothermic on Co(fcc)@N-Gr whereas the Co(fcc)@Gr system shows significantly large energy barrier of - 3.43 eV in the last step when generating H₂O(l) (Fig. 1a). With a non-zero bias ($U = 1.23$ eV), most of the elementary ORR steps become thermodynamically unfavoured. (Fig. 1b) The energy barrier at the rate-determining step (RDS) of Co(fcc)@Gr is at the highest free energy uphill (-4.66 eV) in reaction step IV. Based on the energy landscape at $U = 1.23$ eV, we can assume that all elementary steps in ORR will show exothermic when the applied potential decreases. On Co(fcc)@N-Gr, all elementary reaction steps of the O₂

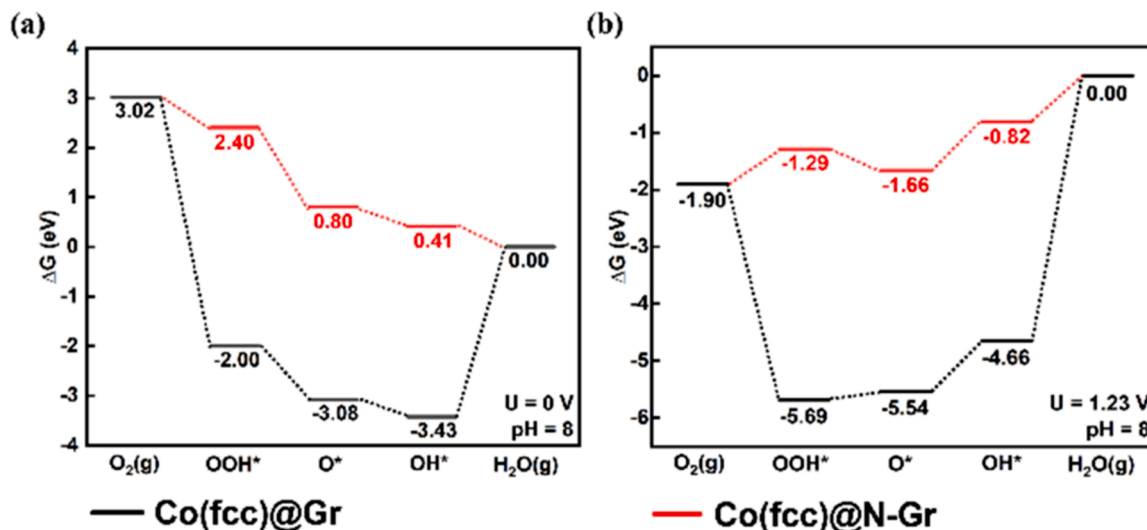


Fig. 1. The calculated free-energy landscape for ORR on Co(fcc)@Gr (black) and Co(fcc)@N-Gr (red) with applied electrode potential (a) $U = 0$ V and (b) 1.23 V at pH 8, respectively.

reduction to H₂O(l) on Co(fcc)@N-Gr are exothermic at $U = 0$ V. When a bias applied at 1.23 V, the reaction step IV ($^*OH + H^+ + e^- + H_2O(l)$) is the most sluggish step with an energy barrier of 0.82 eV, which is comparatively much smaller than that of Co(fcc)@Gr.

3.2. DFT calculation of the built-in electric field of Cobalt (FCC)/N doped carbon

Our recent work demonstrated that the corrosion can be effectively prevented by reducing the surface coverage of the elements which initiate the corrosion reactions, i.e. secondary phase formations with metallic elements of catalyst [32]. Since the reaction activity of a catalyst is generally determined by ion transport, an ideal corrosion-resistive and active ORR catalyst in seawater should repulse Cl⁻ ions and attract H⁺ ions onto its surface. In a cobalt-graphene heterojunction, charge transfer occurs due to the large work function differences between the cobalt core and graphene layers, resulting in improving the electrocatalytic ORR activity.[21] Assume that the charge transfer between multi-layer carbon mainly occurs between the interface of cobalt and carbon layer, the built-in electric field with N-doped monolayer carbon can be calculated. The theoretical electric fields are obtained by the integration of the charge density using following Eq. (1),

$$E = \int_0^{\infty} \frac{\Delta\rho(z)}{\epsilon} dz \quad (8)$$

where $\Delta\rho$ and ϵ are the planar-averaged differential charge density and the dielectric constant of water, respectively. The planar-averaged differential charge was obtained using the following Eq. (2),

$$\Delta\rho(z) = \rho_{Co-Graphene} - \rho_{Co} - \rho_{Graphene} \quad (9)$$

where $\rho_{Co-graphene}$, ρ_{Co} , and $\rho_{graphene}$ are the charge densities of a Co-graphene heterostructure, Co, and graphene, respectively. By the electron transfers between cobalt and graphene and the induced interface dipole moments, the computed electric fields at the active sites of Co(fcc)@N-Gr and Co(fcc)@Gr shown in Fig. 2a. Accordingly, Cl⁻ ions can be repulsed by the strong negative electric fields induced near the catalytic active sites on the surfaces of Co(fcc)@N-Gr and Co(fcc)@Gr. In addition, the pyridinic-N doping in the graphene sheet further increases the strength of the electric field near the encapsulating Co(fcc). We have also considered comparing the difference in charge density of the two possible structures: (1) Co(fcc) with monolayer and (2) multilayer N-Gr. As shown in Fig. 2b, the charge transfer occurs dominantly at the interface between Co(fcc) and N-Gr sheet regardless of the number of N-Gr sheet. Moreover, as the built-in electric field is induced by the interface dipole moment, we also compare the dipole moment of the first N-Gr layer of Co(fcc) in the multilayer N-Gr to that of the monolayer of N-Gr. The dipole moment (\bar{p}) is calculated using the following equation:

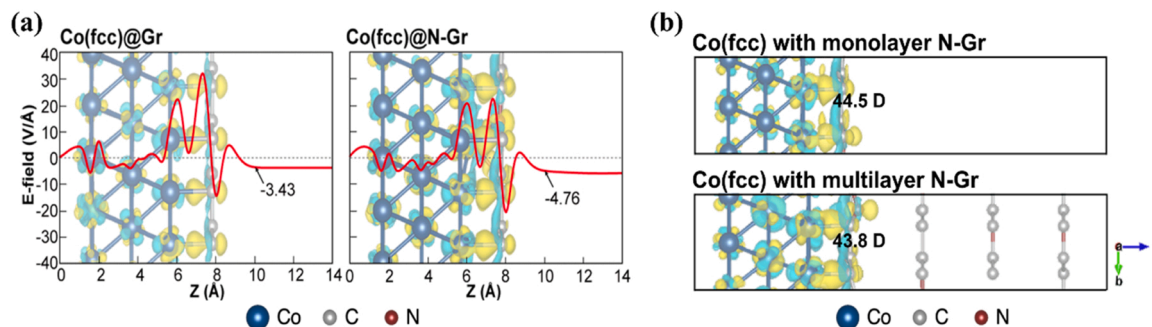


Fig. 2. The calculated electric field of (a) Co(fcc)Gr and Co(fcc)@N-Gr as a function of position in the z-direction with charge density difference. (b) The graphs of plotted charge density difference along z-axis of Co(fcc) with monolayer N-Gr, multilayer N-Gr. The numbers in the graph represent dipole moment (D). The yellow and blue regions represent the electron accumulation and depletion regions, respectively. The value is set at 0.03 e/Bohr. The dark blue, gray and red balls represent Co, C and N atoms, respectively.

$$\vec{p} = - \int_0^z z \Delta \rho(z) dz$$

where $\Delta \rho(z)$ is the planar-averaged differential charge ($\Delta \rho(z) = \rho_{\text{Co-N-Gr}} - \rho_{\text{Co}} - \rho_{\text{N-Gr}}$).

The calculated dipole moment of Co(fcc) with multilayer N-Gr is 43.8 D, which is very close to that of monolayer N-Gr (44.5 D). Accordingly, the number of N-Gr layer should not be considered as a dominant factor. Rather, the first layer of N-Gr has an important role in the formation of built-in electric field at the heterojunction.

Further, the electric field at distance z from the Co/C interface decays with increasing carbon layers/ thickness, according to the general equation:

$$\vec{E}_{\text{dipole}}(z) = \frac{1}{4\pi\epsilon_{\text{graphite}}} \cdot \frac{-\vec{p}}{z^3}$$

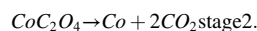
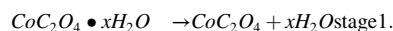
where \vec{p} , z and $\epsilon_{\text{graphite}}$ are the induced dipole moment created from the built-in electric field at the first layer of N-Gr sheet, the length of z -axis, and the permittivity of graphite in c -axis, respectively.

According to Fig. S2, the electrostatic forces on a Cl^- near the surface generated from the built-in electric field is almost twice the magnitude of the concentration gradient (ion diffusion) even when the thickness of N-Gr is increased to 50 Å (5 nm). It indicates that the built-in electric field force (which pushes Cl^- ion away from the surface of catalyst) is overwhelming the diffusion force (which drives Cl^- ion towards the catalyst surface). Therefore, the synergistic effect between the built-in electric field by charge transfer at the interface of the heterojunction and the induced dipole moment by the built-in electric field can significantly improve the Cl repulsion properties of Co(fcc)@N-Gr.

3.3. Structural characterization of Co-N/C catalysts

The details of the Co-N/C fabrication process are shown in Fig. 3. The Co-N/C catalysts are denoted as Co 2 mmol-N/C, Co 3 mmol-N/C, and Co 4 mmol-N/C based on the amount of cobalt salt added into the solution precursor. During the plasma engineering, pyridine decomposed into C_2 and CN radicals and result in direct carbonization of pyridinic-rich N-doped carbon [33]. On the other hand, the concentrated Co oxalate sites were embedded inside the pyridinic-N doped carbon shell instead of directly forming metal particles. Then, the as-synthesized catalysts were heated at 700 °C to calcinate the hydrated cobalt oxalate into nano-sized Co particles. The cobalt nanoparticles were formed

in two stages from hydrate cobalt oxalate as described in the following stages:



The XRD patterns of the as-prepared Co 4 mmol-N/C and heat-treated cobalt catalysts, as shown in Fig. S3, support our hypothesis. The as-prepared Co 4 mmol-N/C catalyst exhibits a distinct peak at around 18°, attributed to hydrated cobalt oxalate ($\text{CoC}_2\text{O}_4 \cdot \text{H}_2\text{O}$, JCPDS 25-250) instead of the expected peak from metallic Co (Fig. S3a). After heat treatment at 700 °C, the embedded cobalt oxalates are successfully calcinated to form face-centered cubic (FCC) metallic cobalt (Co, JCPDS 1-1255) at 44.2° with a dominant (111) crystal plane (Fig. S3b).

To better understand the calcination of the hydrated cobalt oxalate inside the N-doped carbon, TGA was performed at 5 °C/min from 25° to 800 °C in a nitrogen atmosphere, as shown in Fig. S4. The cobalt catalysts show evident thermal decomposition between 150 and 300 °C, which agrees with the values of hydrated cobalt oxalate reported in the literature [34,35]. The weight loss between 400 and 450 °C confirms the thermal decomposition of pyridinic-N carbon shell. The differences in mass reduction corresponding to the concentration of hydrated cobalt oxalate between Co 2 mmol-N/C and Co 4 mmol-N/C, in accordance to the cobalt concentration measured by ICP-OES in Table S1 [36]. Based on the result of ICP-OES, the cobalt concentration increases from 28 wt % to 48 wt% with increasing amount of cobalt precursor (2–4 mmol).

The morphologies of Co 4 mmol-N/C catalyst are investigated in detail by TEM in Figs. 4 and S5. The images show that 20–40 nm-sized cobalt nanoparticles are well-dispersed and embedded in the carbon shell without severe agglomeration, even at a high metal loading of 48 wt%. Also, no significant difference in morphology between Co 2–4 mmol-N/C is being observed in Fig. S6. Fig. 4b–d clearly demonstrate that the graphite-like carbon covered the cobalt nanoparticles. The planar distance of the metal particles is calculated to be 0.205 nm, which corresponds to the crystal plane of Co (111) from the selected area electron diffraction (SAED) image (Fig. 4e). The thickness of the surrounding carbon shell is 0.34 nm, corresponding to graphitic carbon (002). The XRD patterns of Co-N/C catalysts reported in Fig. S3b confirm the presence of fcc metallic Co (JCPDS 1–1255) with a dominant (111) crystal plane at 44.2°, in agreement with SAED image. Furthermore, the elemental mapping (Fig. 4g) demonstrates successful nitrogen doping within the carbon shell. Previous reports have shown that the N-doped carbon shell contributed many advantages to electrical properties

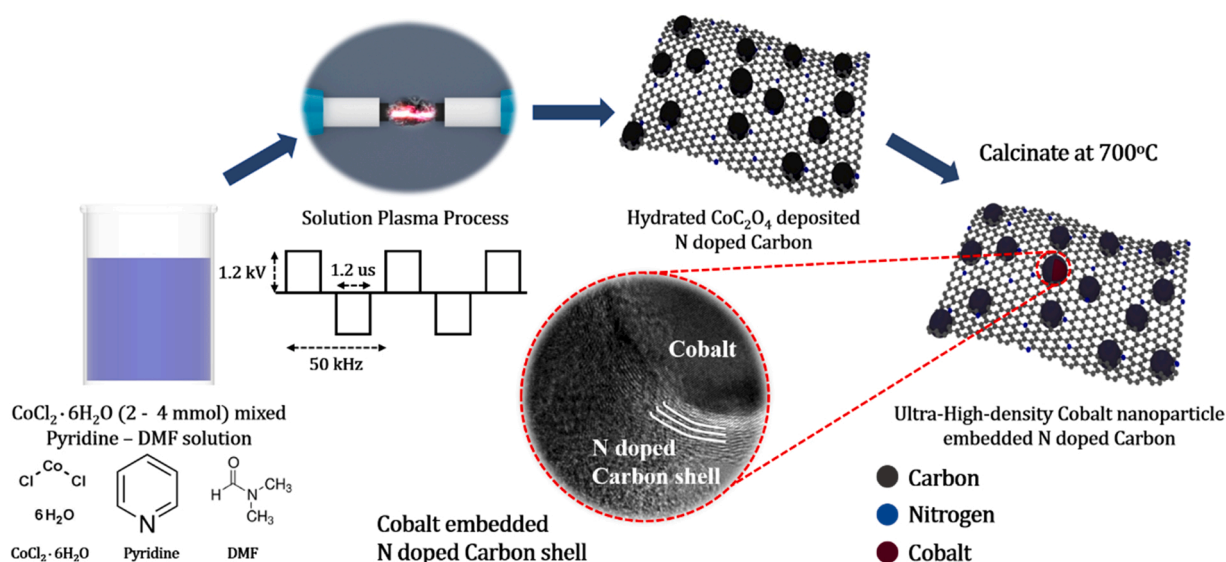


Fig. 3. The synthesis process of Cobalt 2–4 mmol-N/C via plasma engineering.

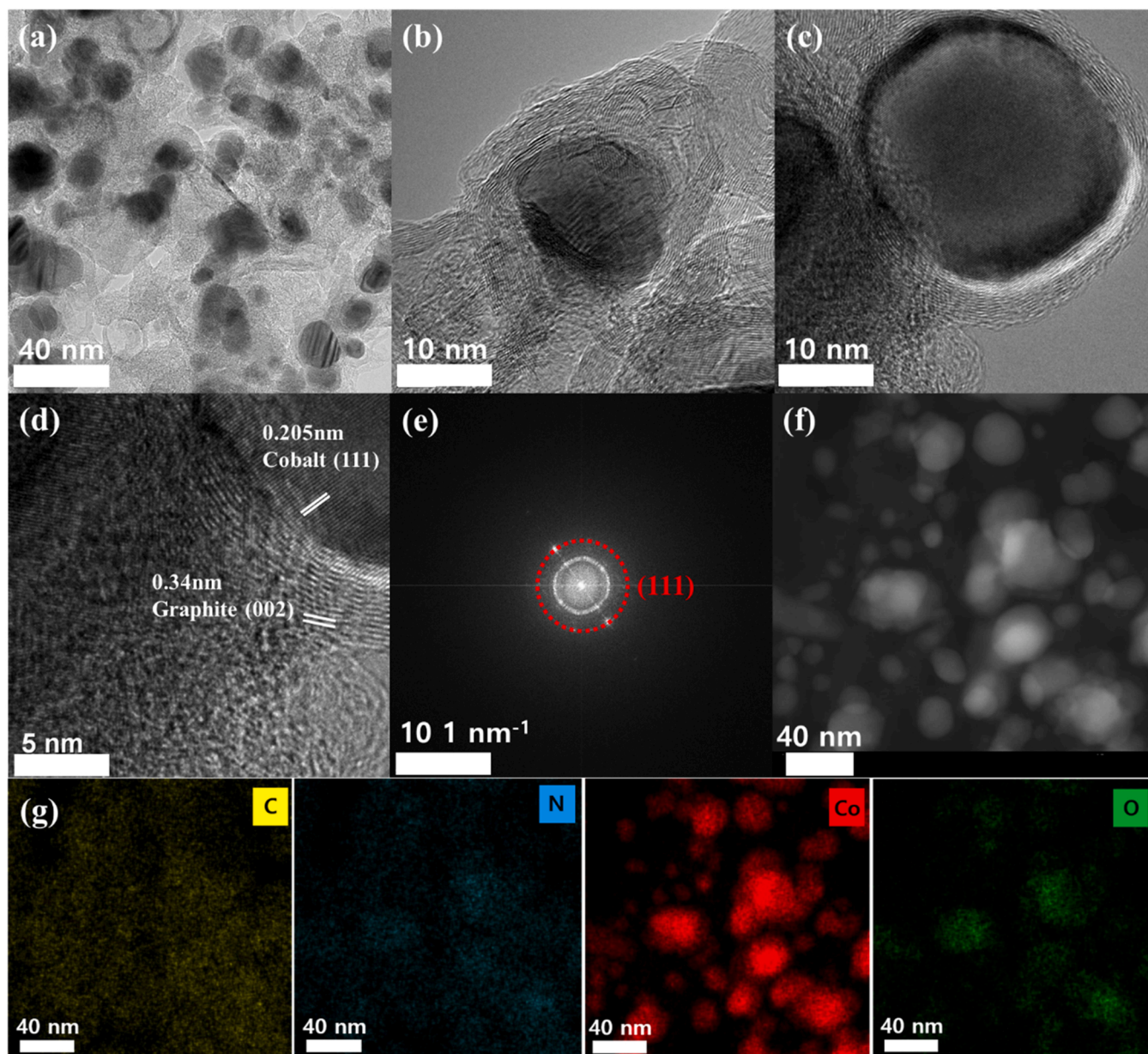


Fig. 4. (a) TEM image of Co 4 mmol-N/C, (b – d) HR-TEM images of Co 4 mmol-N/C in different magnifications, (e) the corresponding SAED image of (c), (f) HADDF-STEM image of Co 4 mmol-N/C, (g) the corresponding EDS mapping of (f).

and the stability of the metal nanoparticle [37]. The BET surface area and micropore ratio of the as-synthesized Co 2–4 mmol-N/C catalysts were measured and are reported in Table S2. The surface area of the catalysts reduce as the Co metal loading increases. The decrease in the surface area is primarily due to the blockage of the pores on the N-doped carbon substrate by cobalt particles, which also explains the decrease in the micropore ratio [38].

The XPS spectra were obtained to understand the chemical properties of the N-doped carbon and cobalt particles in the Co 2–4 mmol-N/C catalysts. In Fig. 5a, each catalyst exhibits a cobalt peak at approximately 775.0 eV and a nitrogen peak at approximately 400.0 eV, while no Cl peaks can be observed. The result confirms that all chloride residues were evaporated after the annealing process. In Fig. 5b, the dominant peak in the C 1s spectra of Co 4 mmol-N/C at 284.0 eV corresponds to the graphitic carbon (sp^2 C=C). The subsequent peaks at 285.2 – 285.7 eV, 286.2 – 286.9 eV, and 288.3 – 288.5 eV are contributed to N- sp^2 -C, N- sp^3 -C, and N-C=O bonding, respectively [39,40]. The N 1s spectra of Co 4 mmol-N/C is shown in Fig. 5c. Interestingly, among

the five major nitrogen functional groups, pyridinic-N bonding (398.6 eV) is dominant in the N-doped carbon. Our previous study reported that plasma engineering allows selective nitrogen bonding through controlling the solution precursors [41]. Other C–N chemical bonds, including pyrrolic-N (399.6 eV), pyridonic-N (400.08 eV), graphitic-N (401.1 eV), and pyridine N-Oxide bonds (403.3 eV) are found co-exist with pyridinic-N. Also, the peak between 404.2 eV and 407.0 eV likely features the $\pi-\pi^*$ satellites of the aromatic C–N groups [39,42–45]. The oxidation states of Co are shown in Fig. 5d. There are two pairs of Co $2p_{1/2}$ and Co $2p_{3/2}$ at their respective binding energies of approximately 779.0 and 794.0 eV. The deconvoluted Co 2p spectra indicates that the metal core mainly shows the oxidation state of Co^{2+} at 780.1 eV, followed by metallic cobalt Co^0 at 778.2 eV and its satellite peaks [44]. On the other hand, the XRD pattern indicates the presence of metallic Co nanoparticles, rather than Co oxide. The Co^{2+} oxidation state is thus mainly due to the surface oxidation of cobalt by the atmospheric environment. The XPS spectra of the Co 2–4 mmol-N/C catalysts (Fig. S7) show similar trends, in which pyridinic-N bonding is dominant

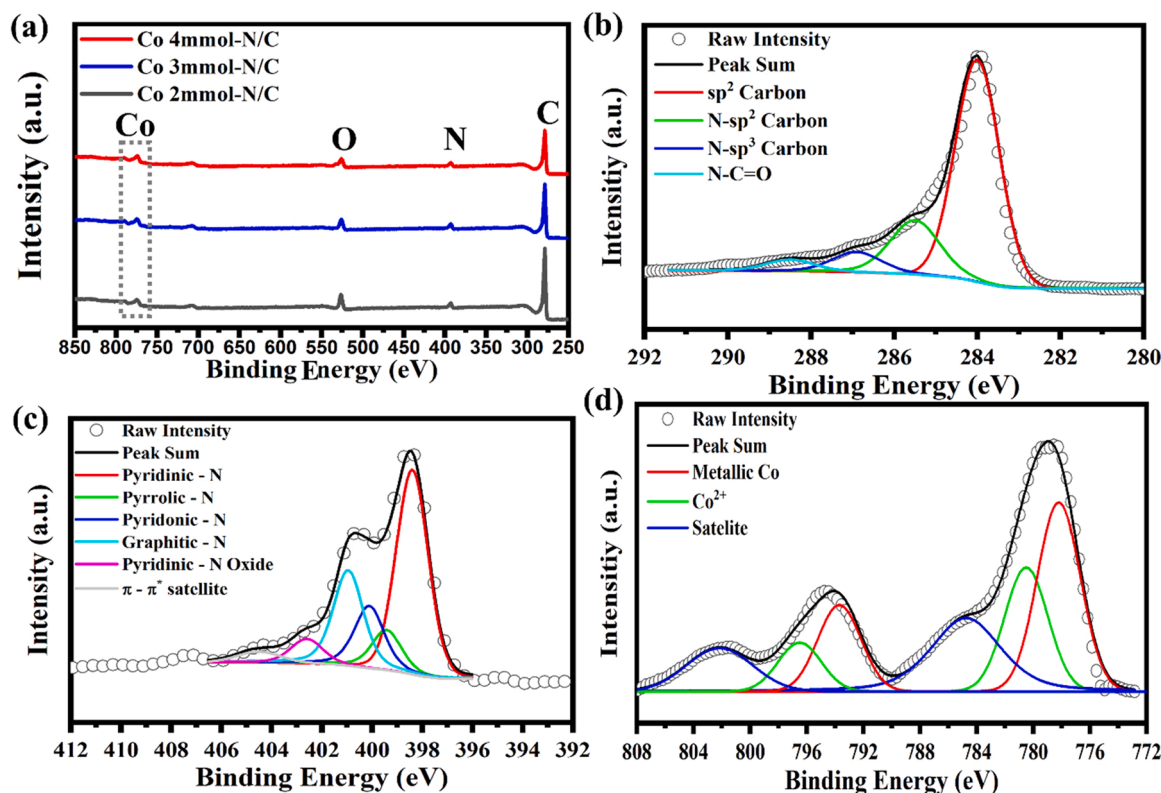


Fig. 5. XPS spectra of (a) wide survey of Co 2–4 mmol-N/C, narrow scans of (b) C 1s, (c) N 1s and (d) Co 2p in Co 4 mmol-N/C.

and Co^{2+} and Co^0 cobalt peaks are co-present.

3.4. Electrochemical catalytic activity in alkaline electrolyte

The electrochemical catalytic activity was measured using a three-electrode system. Fig. 6 shows the ORR performance of the Co 2–4 mmol-N/C catalysts and 20 wt% Pt/C in 0.1 M KOH. In Fig. 6a, Co 4 mmol-N/C exhibits an ORR half-wave potential ($E_{1/2}$) of 0.856 V vs. RHE and a limiting current density of 6.5 mA cm^{-2} , which is better than that of 20 wt% Pt/C (0.854 V vs. RHE, 6.0 mA cm^{-2}). Co 3 mmol N/C also showed relatively high ORR catalytic activity with a half-wave potential of 0.840 V vs. RHE and a limiting current density of 6 mA cm^{-2} . In contrast, Co 2 mmol-N/C showed a comparatively low limiting current density of 3 mA cm^{-2} . To obtain the kinetic parameters of Co 4 mmol-N/C, LSV analysis was performed from 625 rpm to 2025 rpm (Fig. 6b). The onset potential of Co 4 mmol-N/C is 0.95 V vs. RHE, where the calculated K-L plot (Fig. S8) indicates the electron transfer number is close to 4 with a high selectivity of the four-electron reaction pathway. The Tafel slope (Fig. 6c) decreases with increasing cobalt concentration (Co 2 mmol-N/C: 72 mV dec^{-1} , Co 3 mmol-N/C: 74 mV dec^{-1} , Co 4 mmol-N/C: 82 mV dec^{-1}), and all the Co-based catalysts show higher kinetics than the 20 wt% Pt/C (94 mV dec^{-1}). Also, Co 4 mmol-N/C exhibits only 7% decrease in the current density after adding 3 M CH_3OH (Fig. S9). By embedding the cobalt core in a carbon shell, the work function is reduced and therefore promote the adsorption of oxygen to form OOH species. Consequently, the ORR kinetics of the electrocatalyst can be improved [46]. The OER catalytic activity was performed to evaluate the bifunctionality of Co 2–4 mmol-N/C electrocatalysts. As shown in Fig. 6d, the OER performance of the as-synthesized catalysts increases with higher metal concentration. The Co 4 mmol-N/C shows the lowest overpotential of 1.63 V vs. RHE at $j = 10 \text{ mA cm}^{-2}$, whereas Co 2 and 3 mmol-N/C exhibit similar OER activity (1.644 V vs. RHE and 1.65 V vs. RHE, respectively). In addition, the Tafel slope (Fig. 6e) decrease from 105 to

100 mV dec^{-1} with increasing cobalt concentration, similar to the trend in ORR. Most importantly, the bifunctionality performance ΔE (ORR half-wave potential – OER potential at 10 mA cm^{-2}) of our catalysts are summarized in Fig. 6f. The ΔE in ascending order can be summarized as: Co 4 mmol-N/C (0.774 V vs. RHE) < Co 3 mmol-N/C (0.804 V vs. RHE) < Co 2 mmol-N/C (0.81 V vs. RHE) < 20 wt% Pt/C (0.928 V vs. RHE). The excellent bifunctional performance of Co 2–4 mmol-N/C is attributed to the abundant active sites generated from the pyridinic-N and cobalt core interfacial bonding [47]. Table S3 summarizes the ORR/OER performance of our best electrocatalyst and other recently reported bifunctional catalysts. Based on the comparison, Co 4 mmol-N/C shows not only superior ORR activity but also highly competitive bifunctional performance compared to other recently reported electrocatalysts in alkaline electrolytes.

3.5. Electrochemical catalytic activity in seawater electrolyte

After demonstrating the superior catalytic activities of the as-synthesized catalysts in alkaline electrolyte, we performed the same electrochemical analyses in seawater electrolyte to extend their potential as electrocatalysts in rechargeable SWBs. The electrocatalytic ORR catalytic activities of Co 2–4 mmol-N/C and 20 wt% Pt/C in seawater electrolyte are shown in Fig. 7a–c. As expected, Co 4 mmol-N/C catalyst presents the highest ORR activity among the synthesized catalysts (Fig. 7a) with a ORR half-wave potential of 0.7 V vs. RHE, followed by Co 3 mmol-N/C (0.68 V vs. RHE) and Co 2 mmol-N/C (0.657 V vs. RHE). Fig. 7b shows the LSV curves of Co 4 mmol-N/C from 625 to 2025 rpm in the seawater electrolyte. From the curves, the onset potential of Co 4 mmol-N/C is determined to be $\sim 0.8 \text{ V}$ vs. RHE, and the limiting current reached up to 4.5 mA cm^{-2} at 2025 rpm. Fig. 7c shows the Tafel slopes of Co 2–4 mmol-N/C and 20 wt% Pt/C, which are calculated from their corresponding LSV curves. Interestingly, all Co-N/C catalysts show negligible changes in the Tafel slopes ($87\text{--}93 \text{ mV dec}^{-1}$) while the Tafel slope of Pt/C significantly increases to 159 mV dec^{-1}

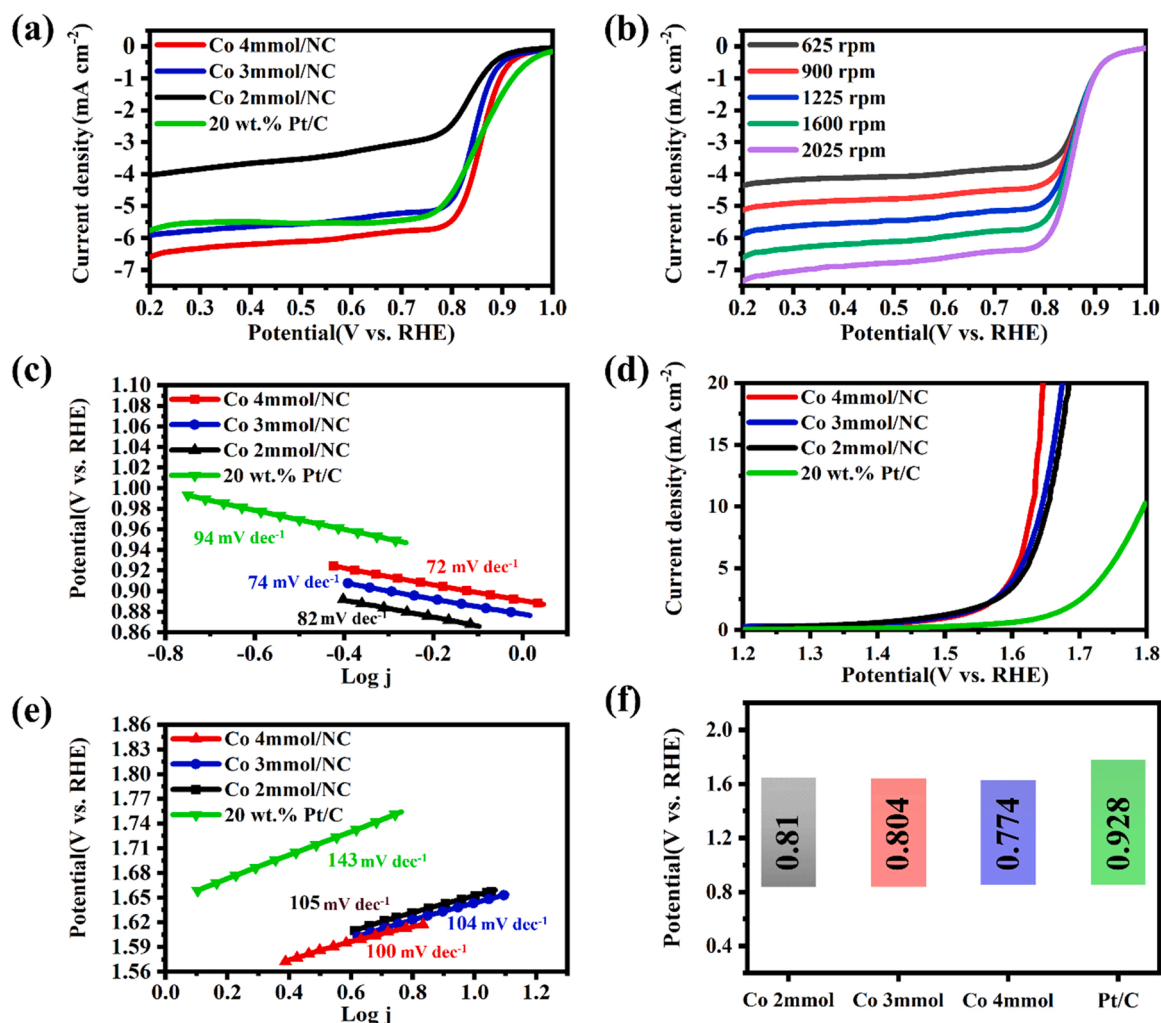


Fig. 6. The electrocatalytic ORR activity of as-synthesized Co 2–4 mmol-N/C and 20 wt% Pt/C in O₂ saturated 0.1 M KOH, (a) LSV curve at 1600 rpm at scan rate of 5 mV s⁻¹, (b) LSV curve of cobalt 4 mmol-N/C from 625 to 2025 rpm at scan rate of 5 mV s⁻¹, (c) Tafel sloped derived from (a); The electrocatalytic OER activity of as-synthesized Co 2–4 mmol-N/C and 20 wt% Pt/C in N₂ saturated 0.1 M KOH, (d) LSV curve at 1600 rpm at scan rate of 5 mV s⁻¹, (e) Tafel slope derived from (d), (f) ORR and OER voltage differences of all catalysts (ΔE : OER $E_{j=10 \text{ mA cm}^{-2}}$ - ORR $E_{1/2}$).

dec⁻¹ compared to the value estimated under alkaline solution. As mentioned above, Cl⁻ ions are easily adsorbed on the metal surface, block the active sites, and thus decrease the ORR reaction kinetics. The adsorbed Cl⁻ ions could affect the O-O bond breaking, and consequently change the first charge transfer step to $\text{O}_2 + e^- = \text{O}_2^-$. The Tafel slope of 20 wt% Pt/C is therefore significantly increased due to the reduction in electron transfer at the ORR rate-determining step (RDS) on Pt surface [48]. To investigate the effect of Cl⁻ adsorption on the electrocatalyst in more detail, the CV profiles under O₂- and N₂ saturated seawater and 0.1 M KOH of Co 4 mmol-N/C and 20 wt% Pt/C are compared in Fig. S10. The cathodic peak current of 20 wt% Pt/C is obviously reduced in the seawater electrolyte (Fig. S10 a–b) [14,15]. On the other hand, Co 4 mmol-N/C, which is composed of metallic cobalt cores surrounded by thin layers of pyridinic-N carbon shell, shows distinct cathodic peaks in both alkaline and seawater electrolyte (Fig. S10 c–d). Furthermore, the effect of pyridinic-N carbon shell on Cl⁻ repulsion is also compared to that of the pristine carbon layer. Cobalt nanoparticles surrounded by pristine carbon shell (denoted as Co 4 mmol/C) was synthesis via an identical procedure with slight modification of the precursor (4 mmol cobalt oxalate added into the benzene precursor). Fig. S11 (a) and (b) show the CV of Co 4 mmol-N/C and Co 4 mmol/C, respectively, under 0.1 M KOH and 0.1 M KOH + 0.5 M NaCl electrolyte. Accordingly, the peak current density corresponding to ORR reaction in Co 4 mmol-N/C

decreases 8% while Co 4 mmol/C further reduces to 12% upon the addition of 0.5 M NaCl (Table S5). The experimental result agrees with the prediction based on DFT theoretical calculation, where a stronger built-in electric field at the interface of Co(fcc)@N-Gr could repel negative Cl⁻ ion more effectively than Co(fcc)@Gr. Therefore, pyridinic-N carbon shell is a successful approach to prevent Cl⁻ adsorption on the ORR active sites and protect the Co core from the corrosive seawater environment.

The electrocatalytic OER activity in seawater electrolyte was further investigated in reported in (Fig. 7d). Co 4 mmol-N/C shows the lowest potential (1.858 V vs. RHE) at 10 mA cm⁻² and outperforms 20 wt% Pt/C (1.878 V vs. RHE), followed by Co 3 mmol-N/C (1.888 V vs. RHE) and Co 2 mmol-N/C (1.948 V vs. RHE). In addition, 20 wt% Pt/C exhibits a higher Tafel slope (139 mV dec⁻¹) than all Co-N/C catalysts (119–143 mV dec⁻¹), which implies that PGM-based catalysts has lower OER kinetics in seawater electrolyte. The remarkable OER performance in Co-N/C demonstrates that the charge transfer resistance is successfully reduced in Co-N/C by the present of abundant active sites and the cobalt/ N-doped graphene interface [49]. Finally, the bifunctional catalytic performance (ΔE) of each catalyst is summarized in Fig. 7f. Co 4 mmol-N/C catalyst again exhibits the lowest ΔE of 1.167 V vs. RHE among all as-synthesized catalysts, which is almost similar to that of 20 wt% Pt/C (1.122 V vs. RHE). As a result, Co 4 mmol-N/C is worth

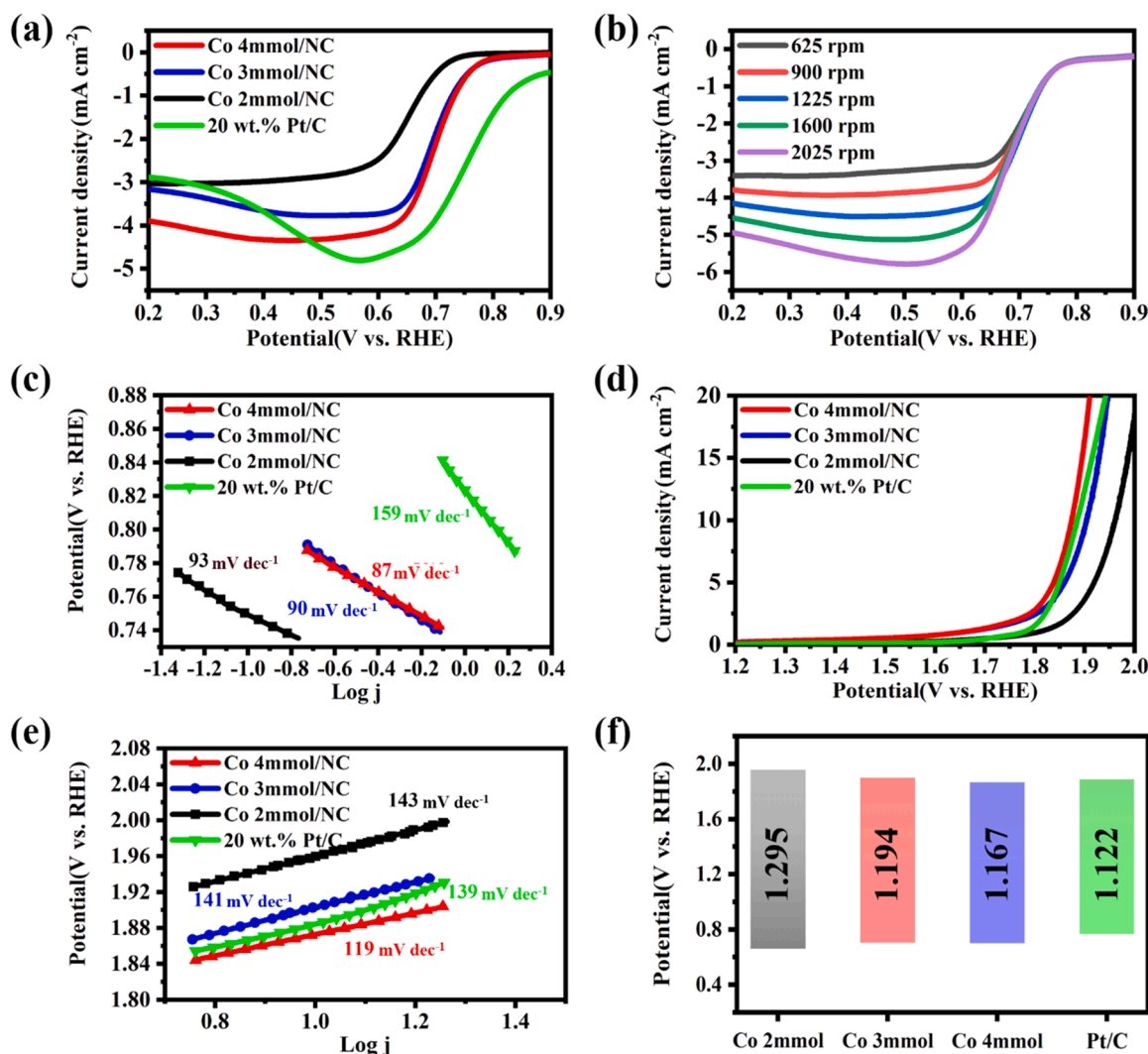


Fig. 7. The electrocatalytic ORR activity of as-synthesized Co 2 – 4 mmol-N/C and 20 wt% Pt/C in O₂ saturated seawater electrolyte, (a) LSV curve at 1600 rpm at scan rate of 5 mV s⁻¹, (b) LSV curve of cobalt 4 mmol-N/C from 625 to 2025 rpm at scan rate of 5 mV s⁻¹, (c) Tafel slope derived from (a); The electrocatalytic OER activity of as-synthesized Co 2 – 4 mmol-N/C and 20 wt% Pt/C (d) LSV curve at 1600 rpm at scan rate of 5 mV s⁻¹ in N₂ saturated seawater electrolyte, (e) Tafel slope derived from (d), (f) ORR and OER voltage differences of all catalysts (ΔE: OER E_{j=10 mA cm⁻²} - ORR E_{1/2}).

being tested further as a bifunctional cathode catalyst in a rechargeable SWBs.

3.6. Electrochemical charge/discharge as seawater battery cathode

To evaluate the practical battery performance under seawater electrolyte, Co 4 mmol-N/C was coated on carbon felt and was employed as a cathode catalysts of a half-cell seawater battery. In Fig. 8a, Co 4 mmol-N/C demonstrates highly improved charge and discharge performance compared to bare carbon felt in a 1-h 0.1-mA charge-discharge cycle. Co 4 mmol-N/C shows discharge and charging voltages of 3.02 V and 3.58 V, respectively, at its initial charge-discharge cycle. Although 20 wt% Pt/C exhibits a similar discharge voltage of 3.08 V at its first discharge, the charging voltage (3.81 V) is much higher than that of Co 4 mmol-N/C. The obtained voltage gap during charge-discharge is calculated as 0.56 V for Co 4 mmol-N/C and 0.73 V for 20 wt% Pt/C, demonstrating that Co 4 mmol-N/C has a much better charge-discharge performance in practical seawater batteries. Furthermore, Fig. 8b compares the long-term stability of three cathode materials during 100 h charge-discharge cycling test. Fig. 8c shows that the voltage gap of Co 4 mmol-N/C increased to 0.62 V, while the voltage gap of 20 wt% Pt/C increases to 0.84 V at the end of the durability test (100 hrs). The result

confirms that Co 4 mmol-N/C has exceptionally high stability during long-term operation in seawater electrolyte. Fig. 8d shows the rate performance of Co 4 mmol-N/C measured with increasing current from 0.02 mA to 0.2 mA. The voltage gaps of the as-synthesized catalyst are reported as 0.24 and 0.85 V at 0.02 and 0.2 mA, respectively. Fig. 8e and Table S4 compare the charge-discharge performance Co 4 mmol-N/C with other recently reported electrocatalysts in SWBs. Our reported catalyst shows superior performance at both low and high currents than other reported PGM-free catalysts. In addition, the performance of Co 4 mmol-N/C is even competitive to those of PGM-based catalysts, such as 50 wt% Pt/C and RuPOM/KB catalyst [8,19,22,50–52].

3.7. Investigation of the protection role of pyridinic-N doping few-layer graphene shell after 100-hr charge-discharge reaction

The morphologies of the used Co 4 mmol-N/C after 100 h cycles in SWBs are illustrated in Fig. 9(a–c). Compared to the fresh catalyst in Fig. 4, the morphology of Co 4 mmol-N/C shows no apparent changes, and the N-doped carbon shell is well maintained after a continuous charge-discharge cycling test. Most importantly, the cobalt core remains highly crystalline and well-protected by the pyridinic-N carbon shell after 100 cycles. Besides the morphology, the differences in chemical

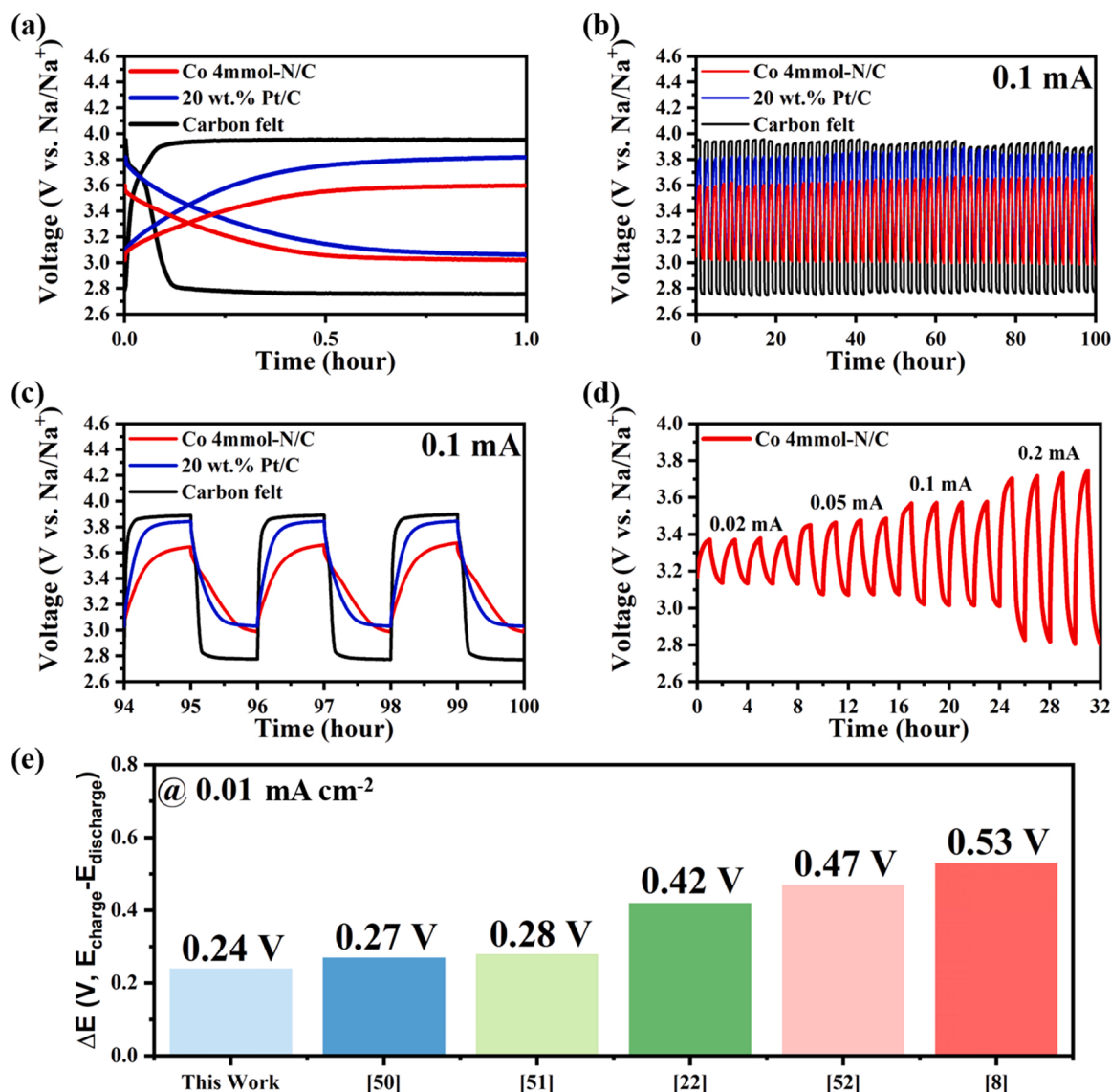


Fig. 8. Electrochemical performance of a half-cell SWBs with cathode catalyst composed of bare carbon felt substrate, Co 4 mmol-N/C, and 20 wt% Pt/C (a) voltage vs. time profiles at 0.1 mA for charge-discharge (b) Cycling stability at 0.1 mA for 100 h, (c) voltage vs. time profiles at the last 3 cycles. (d) rate performance of Co 4 mmol-N/C catalyst in current ranges from 0.02 mA to 0.2 mA. (e) Comparison of bifunctional catalytic performance in SWB between Co 4 mmol-N/C and other reported SWB cathode catalysts.

bonding structures of Co 4 mmol-N/C are also investigated by XPS surface spectra. The C 1 s spectrum of Co 4 mmol-N/C (Fig. 9d) is almost identical to that of the as-prepared sample. On the other hand, the N 1 s spectra after the cycle test (Fig. 9e) significantly differs from the fresh catalyst. Before the cycle test, pyridinic-N derived from pyridine precursor was the dominant nitrogen functional group in the as-synthesized Co 4 mmol-N/C. However, the major peak has shifted to pyridonic-N after 100 discharge-charge cycles. Based on the surface element analysis, the total N content remains relatively constant after the durability test (1.46 and 1.50 at% for fresh and used catalysts, respectively). On the other hand, the surface oxygen atomic percentage increases greatly from 5.08 at% to 10.36 at% after 100 hrs cycle test. The O 1 s spectra between the fresh and used 4 mmol-N/C is compared in Fig. S12. The relative percentage of C-OH also increases accordingly after the continuous charge-discharge process. Guo et al. reported that the surface pyridinic-N firstly created a Lewis-based site and acted as the ORR active site. Then, the oxygen was absorbed at the carbon next to the pyridinic-N as *O and further transferred to *OH, whereas the pyridinic-N was subsequently converted to the pyridonic-N during ORR process [53].

Table S6 summarizes the relative percentage of pyridinic-N, pyridonic-N and C-OH of 4 mmol-N/C before and after the durability test. It is clear that most of the pyridinic-N was converted to the pyridonic-N, and more OH group was absorbed on the carbon surface as C-OH, which agrees to other previous literatures [54–56]. Instead of being transformed to oxidized cobalt species, the narrow scan of Co 2p in the recycled catalyst shows a major peak of metallic Co⁰, suggesting that the cobalt core remains stable under long-term operation (Fig. 9f). This result clearly indicates that the pyridinic-N graphene shell affords various advantages in terms of selective repulsion of Cl⁻ ions as well as protecting the Co active sites from the corrosive seawater environment (Fig. 9g).

4. Conclusion

To realize renewable energy systems such as seawater batteries (SWB), high-performance and high seawater tolerant electrocatalysts are crucial. We have designed and synthesized pyridinic-N doped graphene shell encapsulated cobalt catalysts with a negative surface charge

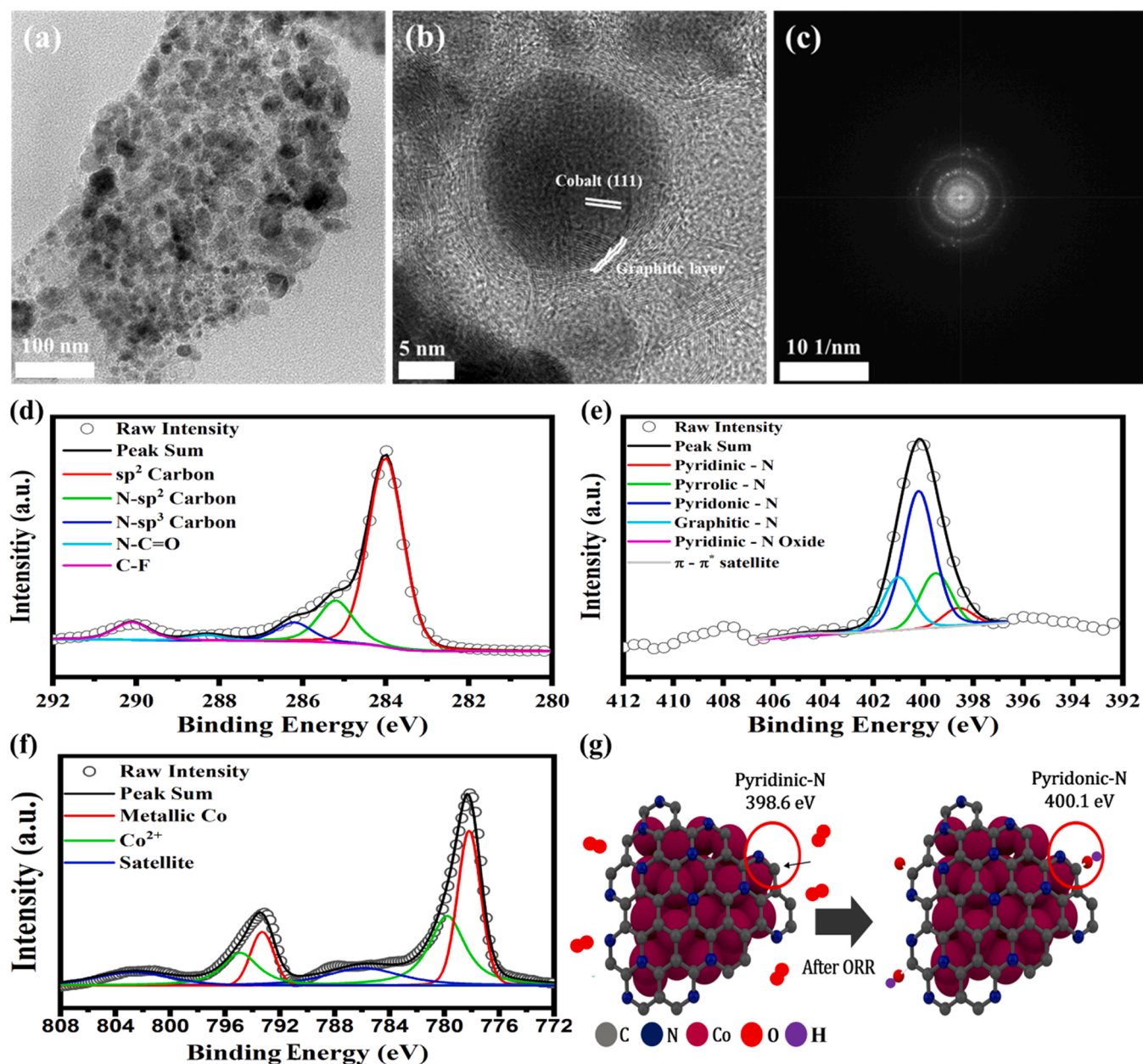


Fig. 9. (a) Low magnification TEM, (b) HR-TEM, (c) SAED images corresponding to (b), (d) XPS narrow scan of C 1s, (e) N1s, (f) Co 2p and (g) schematic of the transformation of pyridinic-N to pyrrolic-N in Co 4 mmol-N/C after cycling test.

to contribute enhanced ORR/OER activity with selective repulsion of Cl^- ions in seawater electrolyte. Based on the DFT calculation on the built-in electric field, we have proved that pyridinic-N doped graphene could significantly promote and strengthen the electric field of the Co-N/C surface, where Cl^- ions can be repulsed by the strong negative electric fields induced near the surface of the active catalytic sites of Co-N/C. This novel approach provides a new branch of the DFT calculation-based catalysts design principle to avoid corruptions or promote ion transports near catalyst surfaces. Experimentally, Co 4 mmol-N/C demonstrated an extremely low overpotential (0.56 V) during the 1st charge-discharge cycle and superior stability with a mere 10% increase of voltage gap after 100 h in rechargeable SWBs. These results provide new design criteria and facile synthesis route for further developing superior and stable cathodic electrocatalyst in corrosive seawater electrolytes. It will be suitable for a wide range of applications, not only rechargeable SWBs but also metal-air batteries exploiting seawater-based electrolytes and seawater electrolysis for hydrogen production

in the near future.

CrediT authorship contribution statement

Seonghee Kim: Methodology, Writing – original draft preparation. **Seulgi Ji:** Writing – original draft preparation. **Hyeonsu Yang:** Visualization, Investigation. **Hyunjee Son:** Investigation. **Heechae Choi:** Software, Writing – Review & Editing. **Jun Kang:** Visualization, Investigation. **Oi L. Li:** Conceptualization, Methodology, Supervision, Writing – Review & Editing.

Declaration of Competing Interest

The authors declare that they have no known competing financial interests or personal relationships that could have appeared to influence the work reported in this paper.

Acknowledgements

O.L.Li acknowledges the financial support by the National Research Foundation of Korea (2021R1I1A30523201262182065300102) and Busan Innovation Institute of Industry, Science & Technology Planning (BISTEP); MJ and HC acknowledge the financial support of Federal Ministry of Education and Research (BMBF) under the "Make Our Planet Grät Again – German Research Initiative" (MOPGA-GRI), 57429784, Implemented by the German Academic Exchange Service Deutscher Akademischer Austauschdienst (DAAD). This research was supported by Basic Science Research Program through the National Research Foundation of Korea(NRF) funded by the Ministry of Education (2021R1I1A3052320)

Appendix A. Supporting information

Supplementary data associated with this article can be found in the online version at [doi:10.1016/j.apcatb.2022.121361](https://doi.org/10.1016/j.apcatb.2022.121361).

References

- [1] V. Das, S. Padmanaban, K. Venkitesamy, R. Selvamuthukumar, F. Blaabjerg, P. Siano, Recent advances and challenges of fuel cell based power system architectures and control – a review, *Renew. Sustain. Energy Rev.* 73 (2017) 10–18, <https://doi.org/10.1016/j.rser.2017.01.148>.
- [2] Y.J. Wang, W. Long, L. Wang, R. Yuan, A. Ignaszak, B. Fang, D.P. Wilkinson, Unlocking the door to highly active ORR catalysts for PEMFC applications: polyhedron engineered Pt-based nanocrystals, *Energy Environ. Sci.* 11 (2018) 258–275, <https://doi.org/10.1039/C7EE02444D>.
- [3] S. Ratso, I. Kruusenberg, M. Kaarik, M. Kook, L. Puust, R. Saar, G. Leis, K. Tammeveski, Highly efficient transition metal and nitrogen co-doped carbide-derived carbon electrocatalysts for anion exchange membrane fuel cells, *J. Power Sources* 375 (2018) 233–243, <https://doi.org/10.1016/j.jpowsour.2017.08.046>.
- [4] X. Wang, Z. Liao, Y. Fu, C. Neumann, A. Turchanin, G. Nam, E. Zschech, J. Cho, J. Zhang, X. Feng, Confined growth of porous nitrogen-doped cobalt oxide nanoarrays as bifunctional oxygen electrocatalysts for rechargeable zinc-air batteries, *Energy Storage Mater.* 26 (2020) 157–164, <https://doi.org/10.1016/j.ensm.2019.12.043>.
- [5] C. Guan, A. Sumboja, W. Zhang, Y. Qian, H. Zhang, X. Liu, Z. Liu, D. Zhao, S. J. Pennycook, J. Wang, Decorating Co/CoNx nanoparticles in nitrogen-doped carbon nanoarrays for flexible and rechargeable zinc-air batteries, *Energy Storage Mater.* 16 (2019) 243–250, <https://doi.org/10.1016/j.ensm.2018.06.001>.
- [6] Y. Zhang, J.S. Park, S.T. Senthikumar, Y. Kim, A novel rechargeable hybrid Na-seawater flow battery using bifunctional electrocatalytic carbon sponge as cathode current collector, *J. Power Sources* 400 (2018) 478–484, <https://doi.org/10.1016/j.jpowsour.2018.08.044>.
- [7] M. Abirami, S.M. Hwang, J. Yang, S.T. Senthikumar, J. Kim, W.S. Go, B. Senthikumar, H.K. Song, Y. Kim, A. Metal-Organic, Framework derived porous cobalt manganese oxide bifunctional electrocatalyst for hybrid Na-air/seawater batteries, *ACS Appl. Mater. Interfaces* 8 (2016) 32778–32787, <https://doi.org/10.1021/acsaami.6b10082>.
- [8] Y. Kim, G.T. Kim, S. Jeong, X. Dou, C. Geng, Y. Kim, S. Passerini, Large-scale stationary energy storage: Seawater batteries with high rate and reversible performance, *Energy Storage Mater.* 16 (2019) 56–64, <https://doi.org/10.1016/j.ensm.2018.04.028>.
- [9] J. Han, S.M. Hwang, W. Go, S.T. Senthikumar, D. Jeon, Y. Kim, Development of coin-type cell and engineering of its compartments for rechargeable seawater batteries, *J. Power Sources* 374 (2018) 24–30, <https://doi.org/10.1016/j.jpowsour.2017.11.022>.
- [10] S.M. Hwang, J.S. Park, Y. Kim, W. Go, J. Han, Y. Kim, Y. Kim, Rechargeable seawater batteries-from concept to applications, *Adv. Mater.* 31 (2019), 1804936, <https://doi.org/10.1002/adma.201804936>.
- [11] V. Stamenkovic, N.M. Markovic, P.N. Ross Jr., Structure-relationships in electrocatalysis: oxygen reduction and hydrogen oxidation reaction on Pt(111) and Pt(100) in solutions containing chloride ions, *J. Electroanal. Chem.* 500 (2001) 44–51, [https://doi.org/10.1016/S0022-0728\(00\)00352-1](https://doi.org/10.1016/S0022-0728(00)00352-1).
- [12] T.J. Schmidt, U.A. Paulus, H.A. Gasteiger, R.J. Behm, The oxygen reduction reaction on a Pt/carbon fuel cell catalyst in the presence of chloride anions, *J. Electroanal. Chem.* 508 (2001) 41–47, [https://doi.org/10.1016/S0022-0728\(01\)00499-5](https://doi.org/10.1016/S0022-0728(01)00499-5).
- [13] S. Dresch, T.N. Thanh, M. Klingenhof, S. Bruckner, P. Hauke, P. Strasser, Efficient direct seawater electrolyzers using selective alkaline NiFe-LDH as OER catalyst in asymmetric electrolyte feeds, *Energy Environ. Sci.* 13 (2020) 1725–1729, <https://doi.org/10.1039/D0EE01125H>.
- [14] J. Yu, B.Q. Li, C.X. Zhao, Q. Zhang, Seawater electrolyte-based metal-air batteries: from strategies to applications, *Energy Environ. Sci.* 13 (2020) 3253–3268, <https://doi.org/10.1039/D0EE01617A>.
- [15] F. Dionigi, T. Reier, Z. Pawolek, M. Gliech, P. Strasser, Design criteria, operating conditions, and nickel-iron hydroxide catalyst materials for selective seawater electrolysis, *ChemSusChem* 9 (2016) 962–972, <https://doi.org/10.1002/cssc.201501581>.
- [16] J.G. Vos, T.A. Wenzendonk, A.W. Jeremiasse, M.T.M. Koper, MnOx/IrOx as selective oxygen evolution electrocatalyst in acidic chloride solution, *J. Am. Chem. Soc.* 140 (2018) 10270–10281, <https://doi.org/10.1021/jacs.8b05382>.
- [17] K. Mamtani, D. Jain, A.C. Co, U.S. Ozkan, Investigation of chloride poisoning resistance for nitrogen-doped carbon nanostructures as oxygen depolarized cathode catalysts in acidic media, *Catal. Lett.* 147 (2017) 2903–2909, <https://doi.org/10.1007/s10562-017-2205-3>.
- [18] M. Sharma, J.H. Jang, D.Y. Shin, J.A. Kwon, D.H. Lim, D. Choi, H. Sung, J. Jang, S. Y. Lee, K.Y. Lee, H.Y. Park, N. Jung, S.J. Yoo, Work functional-tailored graphene via transition metal encapsulation as a highly active and durable catalyst for the oxygen reduction reaction, *Energy Environ. Sci.* 12 (2019) 2200–2211, <https://doi.org/10.1039/C9EE00381A>.
- [19] D.H. Suh, S.K. Park, P. Nakhaniyev, Y.S. Kim, S.M. Hwang, H.S. Park, Hierarchically structured graphene-carbon nanotube-cobalt hybrid electrocatalyst for seawater battery, *J. Power Sources* 372 (2017) 31–37, <https://doi.org/10.1016/j.jpowsour.2017.10.056>.
- [20] L.M.R. Keil, F.M. Moller, M. Kiehl, P.W. Kudella, C.B. Mast, Proton gradients and pH oscillations emerge from heat flow at the microscale, *Nat. Commun.* 8 (2017) 1897, <https://doi.org/10.1038/s41467-017-02065-3>.
- [21] K. Takanebe, Photocatalytic water splitting: quantitative approaches toward photocatalyst by design, *ACS Catal.* 7 (2017) 8002–8006, <https://doi.org/10.1021/acscatal.7b02662>.
- [22] D.K. Bediako, Y. Surendranath, D.G. Nocera, Mechanistic studies of the oxygen evolution reaction mediated by a nickel-borax thin film electrocatalyst, *J. Am. Chem. Soc.* 135 (2013) 3662–3674, <https://doi.org/10.1021/ja3126432>.
- [23] A.S. Haile, H.A. Hansen, W. Yohannes, Y.S. Mekonnen, Pyridinic-type N-doped graphene on cobalt substrate as efficient electrocatalyst for oxygen reduction reaction in acidic solution in fuel cell, *J. Phys. Chem. Lett.* 12 (2021) 3552–3559, <https://doi.org/10.1021/acs.jpclett.1c00198>.
- [24] A.A. Bhardwaj, J.G. Vos, M.E.S. Beatty, A.F. Baxter, M.T.M. Koper, N.Y. Yip, D. V. Esposito, Ultrathin silicon oxide overlayers enable selective oxygen evolution from acidic and unbuffered pH-neutral seawater, *ACS Catal.* 11 (2021) 1316–1330, <https://doi.org/10.1021/acscatal.0c04343>.
- [25] S.T. Senthikumar, W. Go, J. Han, L.P.T. Thuy, K. Kishor, Y. Kim, Y. Kim, Emergence of rechargeable seawater batteries, *J. Mater. Chem. A* 7 (2019) 22803, <https://doi.org/10.1039/c9ta08321a>.
- [26] R. Meng, C. Zhang, Z. Lu, X. Xie, Y. Liu, Q. Tang, H. Li, D. Kong, C.N. Geng, Y. Jiao, Z. fan, Q. he, Y. Guo, G. Ling, Q.H. Yang, An oxygenophilic atomic dispersed Fe-N-C catalysts for lean-oxygen seawater batteries, *Adv. Energy Mater.* 11 (2021), 2100683.
- [27] S.M. Hwang, J.S. Park, Y. Kim, W. Go, J. Han, Y. Kim, Y. Kim, Rechargeable seawater batteries-from concept to applications, *Adv. Mater.* 31 (2019), 1804936, <https://doi.org/10.1002/adma.201804936>.
- [28] P. Manikandan, K. Kishor, J. Han, Y. Kim, Advanced perspective on the synchronized bifunctional activities of P2-type materials to implement an interconnected voltage profile for seawater batteries, *J. Mater. Chem. A* 6 (2018) 11012, <https://doi.org/10.1039/C8TA02667J>.
- [29] J.K. Norskov, J. Rossmeisl, A. Logadottir, L. Lindqvist, J.R. Kitchin, T. Bligaard, H. Jonsson, Origin of the overpotential for oxygen reduction at a fuel-cell cathode, *J. Phys. Chem. B* 108 (2004) 17886–17892, <https://doi.org/10.1021/jp047349j>.
- [30] R. Ma, G. Lin, Y. Zhou, Q. Liu, T. Zhang, G. Shan, M. Yang, J. Wang, A review of oxygen reduction mechanisms for metal-free carbon-based electrocatalysts, *Npj Comput. Mater.* 5 (2019) 78, <https://doi.org/10.1038/s41524-019-0210-3>.
- [31] S. Kattel, P. Atanassov, B. Kiefer, A density functional theory study of oxygen reduction reaction on non-PGM Fe-Nx-C electrocatalysts, *Phys. Chem. Chem. Phys.* 16 (2014) 73800, <https://doi.org/10.1039/C4CP01634C>.
- [32] S. Kim, S. Ji, K.H. Kim, S.H. Roh, Y. Cho, C.L. Lee, K.S. Lee, D.G. Choi, H. Choi, J. K. Kim, J.H. Park, Revisiting surface chemistry in TiO₂: a critical role of ionic passivation for pH-independent and anti-corrosive photoelectrochemical water oxidation, *Chem. Eng. J.* 407 (2021), 126929, <https://doi.org/10.1016/j.cej.2020.126929>.
- [33] G. Panomsuwan, S. China, Y. Kaneko, N. Saito, T. Ishizaki, In situ solution plasma synthesis of nitrogen-doped carbon nanoparticles as metal-free electrocatalysts for the oxygen reduction reaction, *J. Mater. Chem. A* 2 (2014) 18677, <https://doi.org/10.1039/C4TA03010A>.
- [34] J. Qi, W. Zhang, R. Cao, Aligned cobalt-based Co@CoOx nanostructures for efficient electrocatalytic water oxidation, *Chem. Commun.* 53 (2017) 9277, <https://doi.org/10.1039/C7CC04609J>.
- [35] J. Xu, L. He, H. Liu, T. Han, Y. Wang, C. Zhang, Y. Zhang, Controlled synthesis of porous anhydrous cobalt oxalate nanorods with high reversible capacity and excellent cycling stability, *Electrochim. Acta* 170 (2015) 85, <https://doi.org/10.1016/j.electacta.2015.04.114>.
- [36] A.T. Khodakov, R. Vechara, A.G. Constant, Fischer-Tropsch synthesis over silica supported cobalt catalysts: mesoporous structure versus cobalt surface density, *Appl. Catal. A Gen.* 254 (2003) 273, [https://doi.org/10.1016/S0926-860X\(03\)00489-7](https://doi.org/10.1016/S0926-860X(03)00489-7).
- [37] W. Shuang, H. Huang, L. Kong, M. Zhong, A. Li, D. Wang, Y. Xu, X.H. Bu, Nitrogen-doped carbon shell-confined Ni3S2 composite nanosheets derived from Ni-MOF for high performance sodium-ion battery anodes, *Nano Energy* 62 (2019) 154–163, <https://doi.org/10.1016/j.nanoen.2019.05.030>.
- [38] D. Nareesh, V.P. Kumar, M. Harisekhar, N. Nagaraju, B. Putrakumar, K.V.R. Chary, Characterization and functionalities of Pd/hydrothermal catalysts, *Appl. Surf. Sci.* 314 (2014) 199, <https://doi.org/10.1016/j.apsusc.2014.06.156>.

- [39] E. Bayram, G. Yilmaz, S. Mukerjee, A solution-based procedure for synthesis of nitrogen doped graphene as an efficient electrocatalyst for oxygen reduction reactions in acidic and alkaline electrolytes, *Appl. Catal. B Environ.* 192 (2016) 26–34, <https://doi.org/10.1016/j.apcatb.201603.043>.
- [40] B.H. Matsoso, K. Ranganathan, B.K. Mutuma, T. Leretholi, G. Jones, N.J. Covile, Time-dependent evolution of the nitrogen configurations in N-doped graphene films, *RSC Adv.* 6 (2016), 106914, <https://doi.org/10.1039/C6RA24094A>.
- [41] S. Kim, H. Park, O.L. Li, Cobalt nanoparticles on plasma-controlled nitrogen-doped carbon as high-performance ORR electrocatalyst for primary Zn-air battery, *Nanomaterials* 10 (2020) 223, <https://doi.org/10.3390/nano10020223>.
- [42] S. Kundu, B. Malik, D.K. Pattanayak, V.K. Pillai, Effect of dimensionality and doping in quasi “One-Dimensional (1-D)” nitrogen-doped graphene nanoribbons on the oxygen reduction reaction, *ACS Appl. Mater. Interfaces* 9 (2017) 38409–38418, <https://doi.org/10.1021/acsami.7b09601>.
- [43] M.E.M. Buan, N. Muthuswamy, J.C. Walmsley, D. Chen, M. Ronning, Nitrogen-doped carbon nanofibers for the oxygen reduction reaction: importance of the iron growth catalyst phase, *ChemCatChem* 9 (2017) 1663–1674, <https://doi.org/10.1002/cctc.201601585>.
- [44] G. Soto, Electron spectroscopic identification of carbon species on CN_x films, *Mater. Lett.* 49 (2001) 352–356.
- [45] M. Li, C. Bao, Y. Liu, J. Meng, X. Liu, Y. Cai, D. Wu, Y. Zong, T.P. Loh, Z. Wang, Reduced graphene oxide-supported cobalt oxide decorated N-doped graphitic carbon for efficient bifunctional oxygen electrocatalysis, *RSC Adv.* 9 (2019) 16534, <https://doi.org/10.1039/C9RA02389E>.
- [46] A. Wang, C. Zhao, M. Yu, W. Wang, Trifunctional Co nanoparticle confined in defect-rich nitrogen-doped graphene for rechargeable Zn-air battery with a long lifetime, *Appl. Catal. B Environ.* 281 (2021), 119514, <https://doi.org/10.1016/j.apcatb.2020.119514>.
- [47] T. Feng, X.R. Zhao, C.K. Dong, H. Liu, X.W. Du, J. Yang, Boosting reversible oxygen electrocatalysis with enhanced interfacial pyridinic-N-Co bonding in cobalt oxide/mesoporous N-doped graphene hybrids, *Nanoscale* 10 (2018) 22140, <https://doi.org/10.1039/C8NR07945E>.
- [48] Y.F. Fang, Z.P. Liu, Tafel kinetics of electrocatalytic reactions: from experiment to first-principles, *ACS Catal.* 4 (2014) 4364–4367, <https://doi.org/10.1021/cs501312v>.
- [49] S. Jeong, K. Hu, T. Ohto, Y. Nagata, H. Masuda, J. Fujita, Y. Ito, Effect of graphene encapsulation of NiMO alloys on oxygen evolution reaction, *ACS Catal.* 10 (2020) 792–799, <https://doi.org/10.1021/acscatal.9b04134>.
- [50] J. Kim, J. Park, J. Lee, W.G. Lim, C. Jo, J. Lee, P. Biomass-Derived, N self-doped hard carbon as bifunctional oxygen electrocatalyst and anode material for seawater batteries, *Adv. Funct. Mater.* 31 (2021), 2010882, <https://doi.org/10.1002/adfm.202010882>.
- [51] K.H. Shin, J. Park, S.K. Park, P. Nakhavivej, S.M. Hwang, Y. Kim, H.S. Park, Cobalt vanadate nanoparticles as bifunctional oxygen electrocatalysts for rechargeable seawater batteries, *J. Ind. Eng. Chem.* 72 (2019) 250–254, <https://doi.org/10.1016/j.jiec.2018.12.025>.
- [52] S.T. Senthilkumar, S.O. Park, J. Kim, S.M. Hwang, S.K. Kwak, Y. Kim, Seawater battery performance enhancement enabled by a defect/dege-rich, oxygen self-doped porous carbon electrocatalyst, *J. Mater. Chem. A* 5 (2017) 14174, <https://doi.org/10.1039/C7TA03298F>.
- [53] D. Guo, R. Shibuya, C. Akiba, S. Saji, T. Kondo, J. Nakamura, Active sites of nitrogen doped carbon materials for oxygen reduction reaction clarified using model catalysts, *Science* 351 (2016) 361, <https://doi.org/10.1126/science.aad0832>.
- [54] Y. Ha, B. Fei, X. Yan, H. Xu, Z. Chen, L. Shi, M. Fu, W. Xu, R. Wu, Atomically dispersed co-pyridinic N-C for superior oxygen reduction reaction, *Adv. Energy Mater.* 10 (2020), 2002592, <https://doi.org/10.1002/aenm.2002592>.
- [55] O. Changrui, C. Hui, W. Hou, L. Yalin, L. Run, L. Hongbo, A novel in situ synthesis of nitrogen-doped graphene with excellent electrocatalytic performance for oxygen reduction reaction, *Electrochim. Acta* 380 (2021), 138256, <https://doi.org/10.1016/j.electacta.2021.138256>.
- [56] N.D.K. Tu, S.O. Park, J. Park, Y. Kim, S.K. Kwak, S.J. Kang, Pyridinic-nitrogen-containing carbon cathode: efficient electrocatalyst for seawater batteries, *ACS Appl. Energy Mater.* 3 (2020) 1602–1608, <https://doi.org/10.1021/acsaem.9b02087>.